2025-01-0312 Published 02 Jul 2025

In Situ Observation of Different Soot Layers in a Model Filter Channel during Its Regeneration

Ole Desens, Fabian P. Hagen, Jörg Meyer, and Achim Dittler Karlsruhe Institute of Technology

Citation: Desens, O., Hagen, F.P., Meyer, J., and Dittler, A., "In Situ Observation of Different Soot Layers in a Model Filter Channel during Its Regeneration," SAE Technical Paper 2025-01-0312, 2025, doi:10.4271/2025-01-0312.

Received: 29 Jan 2025 Revised: 28 Mar 2025 Accepted: 01 Apr 2025

Abstract

In order to comply with increasingly stringent emission regulations and ensure clean air, wall-flow particulate filters are predominantly used in exhaust gas aftertreatment systems of combustion engines to remove reactive soot and inert ash particles from exhaust gases. These filters consist of parallel porous channels with alternately closed ends, effectively separating particles by forming a layer on the filter surface. However, the accumulated particulate layer increases the pressure drop across the filter, requiring periodic filter regeneration. During regeneration, soot oxidation breaks up the particulate layer, while resuspension and transport of individual agglomerates can occur. These phenomena are influenced by gas temperature and velocity, as well as by the dispersity and reactivity of the soot particles. Renewable and biomass based fuels can produce different types of soot with different reactivities and dispersities. Therefore, this study focuses on the influences of soot dispersity and reactivity by varying the reactive particle system. A model wall-flow filter channel is used for the investigation, enabling the observation of the layer break-up and detachment of particle structures from the filter surface over the entire channel length using a high-speed camera operating at 1000 fps. Recordings reveal significant differences in the behavior of the different soot types. Image analysis provides insights into the visual layer break-up, evolution of structure sizes, detachment dynamics, agglomerate velocities, and the spatial and temporal distribution of detachment events. General parameters, such as regeneration time and pressure drop, further characterize the regeneration process. The results provide insights into the detachment and rearrangement behavior of reactive particle structures with varying dispersities and reactivities in wall-flow filters, demonstrating that these characteristics can significantly influence the regeneration process.

Introduction

Environmental protection and air quality are essential for safeguarding human health. The revised EU Air Quality Directive (EU) 2024/2881 [1] sets more stringent limits on key air pollutants, including particulate matter $PM_{2.5}$ and PM_{10} and nitrogen oxides, to further reduce air pollution across Europe. The annual mean limit for fine particulate matter $PM_{2.5}$ has been tightened from 25 $\mu g/m^3$ to 10 $\mu g/m^3$. One focus of the directive is the monitoring requirement of black carbon and ultrafine particles, whose adverse impacts on human health and the climate have been increasingly recognized as critical. Combustion-related particulate emissions represent a significant challenge, requiring efficient mitigation strategies. In modern combustion engines, particulate filters (wall-flow/cross-flow) are indispensable components of exhaust aftertreatment systems, already effectively capturing ash and soot particles to ensure compliance with emission regulations [2, 3]. During operation, diesel particulate filters (DPFs) and gasoline particulate filters (OPFs/GPFs) trap both reactive soot and inert ash particles, with the design of the filter and the separation process directly influencing pressure drop and filtration efficiency [4, 5].

The structure of the deposited particle layer within the filter also affects both flow resistance and particle separation efficiency. In the literature, two main deposition patterns are described as limiting cases: homogeneous layer formation along the entire filter channel length and plug-end filling, where particle accumulation is near the downstream end of the filter channel [6, 7]. While homogeneous layer deposition improves filtration efficiency at the expense of higher backpressure, plug-end filling reduces backpressure but decreases the effective filter length and therefore filtration efficiency [6, 8, 9]. Therefore, periodic filter regeneration is mandatory and realized via high-temperature oxidation that oxidizes soot into CO_2 and CO while leaving incombustible ash residues behind. The

soot layer break-up is a key aspect of particulate filter regeneration, a complex phenomenon which depends not only on operating parameters such as temperature, flow velocity, and layer thickness but also on soot reactivity and dispersity. Elevated temperatures and gas velocities increase particle resuspension [10]. Sappok et al. [11] performed visual inspections of a small diesel particulate filter section during regeneration using optical methods and a stereomicroscope. They observed the initial break-up of the soot layer, where detached particle structures were transported, redeposited, or carried further downstream. However, the exact points of resuspension and whether these structures reached the end of the channel were not clarified. Thieringer et al. [10] investigated the dynamics of soot layer break-up, resuspension, and particle transport in a single wall-flow filter channel. High-speed imaging with high spatial and temporal resolution over the entire length revealed that thicker soot layers tend to form larger particle structures, shifting the resuspension points towards the end of the channel. Higher gas velocities increased resuspension frequency, while elevated temperatures accelerated soot oxidation and reduced regeneration time. These findings emphasize the role of process parameters in influencing soot dynamics during regeneration.

Numerical simulations using Lattice-Boltzmann methods have further shown that particle structure detachment is more likely near the channel inlet, where shear forces are higher, while downstream regions experience lower detachment rates due to diminished flow forces [12].

Previous studies indicate that smaller primary particle sizes of soot are generally associated with higher reactivity [13, 14]. Hagen et al. investigated the reactivity of different soot types, including flame soot, engine combustion soot, and carbon black (CB), under representative oxidation conditions. Their results suggested that soot nanostructure plays a more significant role in reactivity than primary particle size, with CB exhibiting lower reactivity compared to propane-derived soot [15].

In this study, the relationship between layer break-up and rearrangement processes during filter channel regeneration is investigated by comparing highly reactive propane soot (PropSoot) with less reactive CB layers in a model filter channel. Layer break-up, particle detachment, and transport along a model filter channel are analyzed using high-speed imaging.

Materials and Method

Reactive Particulate Systems

To investigate the influence of soot reactivity and dispersity on regeneration and particle rearrangement processes within the model filter channel, two different soot particle systems are chosen. The first system is a highly reactive PropSoot produced by the MiniCAST 6204C soot generator (Jing Ltd., Zollikofen, Switzerland), used in previous studies [10]. The second system is a carbon black (lamb black) sample with larger primary particle size and lower reactivity. Selecting these distinct soot types spans a range of reactivities and dispersities, offering initial insights into the parameters influencing the observed phenomena. Figure 1 presents scanning electron microscopy (SEM) images and corresponding particle size distributions for PropSoot (a, b) and CB (c, d). In the SEM-images individual nanoparticles, aggregated into larger structures, can be clearly identified. The corresponding histograms (right figures) show distinct particle size distributions, with the PropSoot exhibiting a count median diameter (CMD) of approximately 26 nm, while the CB features a CMD of about 101 nm.

The PropSoot particle sizes match those in the literature for soot from different combustion conditions and fuels, including conventional and renewable fuels. According to a series of high-resolution transmission electron microscopy (HRTEM) studies soot particles are nearly spherical primary particles, usually a few tens of nanometers in size, forming larger agglomerates and aggregates [5, 15, 16, 17]. Whereby the CB examined here has larger primary particle diameters on average compared to the literature and the PropSoot. The reactivity of the soot samples was determined using temperature-programmed oxidation (TPO). TPO experiments were performed under dynamic, non-isothermal conditions using a TG 209 F1 Libra thermobalance (Netzsch Gerätebau GmbH, Germany). The initial sample mass was

FIGURE 1 SEM images of (a) PropSoot and (c) CB, recorded at an accelerating voltage of 10.0 kV, a magnification of 100 kX, and a working distance of 5.7 mm. The corresponding particle size distributions (b, d) indicate a CMD of approximately 26 nm for the PropSoot and about 101 nm for the CB.

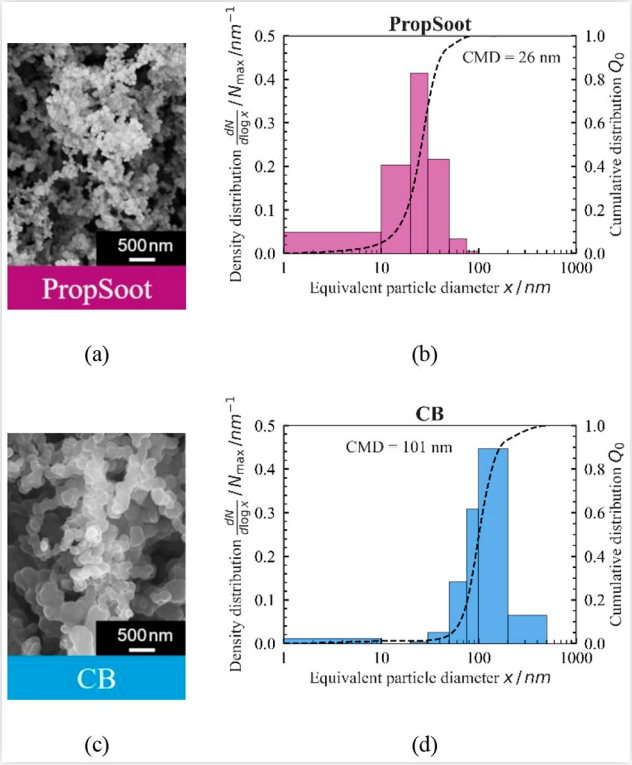

kept constant at m_0 = 2 mg ± 0.2 mg, and the samples were heated from ambient temperature to 1200 K at a constant heating rate of β = 5 K/min under an oxidizing atmosphere consisting of 21 vol. % O_2 and 79 vol. % N_2 at atmospheric pressure. The oxidation rates were obtained from the differential mass loss rate dα/dT, where α represents the fractional mass conversion. The temperature of the maximum oxidation rate, T_{max}, serves as a key indicator of soot reactivity [15]. Experimentally, the TPO profiles exhibit an increase in oxidation rate from the left to T_{max}, which is attributed to the temperature-dependent acceleration of the oxidation reaction. In contrast, to the right of T_{max}, the oxidation rates decrease due to the consumption of the soot sample during the non-isothermal experiment. Lower T_{max} values indicate higher soot reactivity, whereas higher T_{max} values correspond to lower reactivity. The temperature dependency of the oxidation rate was modeled using a global kinetic approach from Hagen et al. [15] based on the Arrhenius equation, expressed as follows:

$$\frac{d\alpha}{dT} = -k_{ox} \cdot \alpha^n = -k_{0,ox} \cdot exp\left(\frac{-E_a}{R \cdot T}\right) \cdot \alpha^n, \quad (1)$$

where k_{ox} is the oxidation rate coefficient, $k_{0,ox}$ is the pre-exponential factor, E_a is the apparent activation energy, n is the overall reaction order, R is the universal gas constant, and T is the temperature. The kinetic parameters were obtained by fitting the model equation to the experimentally determined TGA profiles using the Levenberg-Marquardt method [18, 19].

The TPO profiles of the PropSoot and CB particles in Figure 2 illustrate the temperature-dependent oxidation behavior, represented by the differential mass loss rate dα/dT as a function of temperature. The experimentally determined profiles reveal that the PropSoot particles exhibit a lower temperature at the maximum oxidation rate, T_{max} = 817 K, compared to the CB particles, for which T_{max} is 902 K. This significant difference indicates that PropSoot is more reactive than CB, as oxidation rates remain significant even at lower temperatures. The experimentally determined T_{max} values and the derived activation energies E_a are consistent with those reported for soot particles generated in combustion engines [15, 21, 22, 23]. However, the broader profile observed for PropSoot suggests a slower and more gradual oxidation process, likely due to an inhomogeneous particle structure or composition. In contrast, the sharper peak for CB reflects more uniform oxidation kinetics, albeit at higher temperatures.

The derived kinetic parameters, summarized in the table of Figure 2 on the right, further support these findings. The pre-exponential factor $k_{0,ox}$ for PropSoot ($8.05 \cdot 10^5$ s^{-1}) is lower than that for CB ($3.59 \cdot 10^6$ s^{-1}), despite the lower activation energy E_a of PropSoot (137 kJ/mol) compared to CB (162 kJ/mol). Additionally, the reaction order n for PropSoot (1.39) is higher than that of CB (0.95), indicating differences in oxidation mechanisms and particle reactivity behavior. In summary, the TPO analysis demonstrates that PropSoot is more reactive than CB, as evidenced by its lower T_{max} and activation energy.

Experimental Setup and Procedures

The experimental setup used to investigate layer break-up and particle structure detachment and transport in a model filter channel is shown in Figure 3 The experiment is conducted in three main phases:

1. layer formation,
2. heating up the system under inert gas,
3. switch to oxidation gas and regeneration of the model filter channel.

Particle layers are formed by depositing particles in the model filter channel over a defined time at a constant gas velocity of 13.2 m/s at the channel inlet under ambient temperature conditions. The process parameters for layer formation are summarized in Table 1. Air and nitrogen are supplied via mass flow controllers, and the flow is heated in an oven before entering the model filter channel. Within the heated channel, particles are deposited while the temperature and pressure levels are continuously monitored to ensure well-defined experimental conditions. After layer build-up, a high-speed camera records the layer break-up, particle structure detachment, and transport at

FIGURE 2 Experimentally determined TPO profiles of the PropSoot particles, data from [20], and the CB particles, c_{O2} = 21 vol. %, c_{N2} = 79 vol. %, heating rate β = 5 K/min, and the determined reaction parameters in the table on the right.

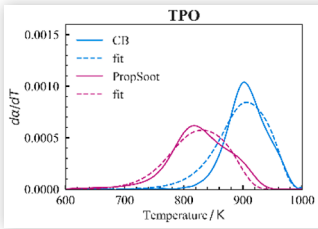

Parameter	Prop-Soot	CB
$k_{0,ox}$ / s^{-1}	$8.05 \cdot 10^5$	$3.59 \cdot 10^6$
E_a / kJ/mol	137	162
n	1.39	0.95
T_{max} / K	817	902

FIGURE 3 Schematic representation of the experimental setup used. On the lower right, a 3D CAD drawing [10] of the channel is shown.

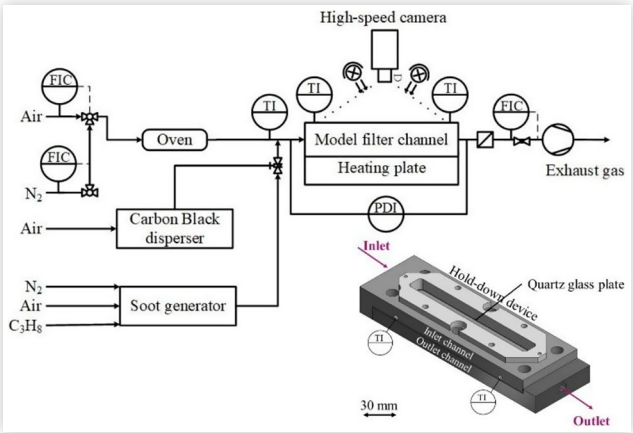

TABLE 1 Process parameters applied for soot layer formation and subsequent regeneration.

Layer Formation		Regeneration	
Parameter	**Value**	**Parameter**	**Value**
Gas velocity (channel inlet) / m/s	13.2	Gas velocity (channel inlet) / m/s	60
Temperature / K	293	Temperature / K	823
Carrier gas	air	Oxidation gas	air
Deposited mass / mg	10 ± 2 mg		

100-1000 fps. The exhaust gas is then passed through a HEPA filter, which removes residual particles before discharging the purified gas. The process parameters for regeneration, outlined in Table 1, are selected to align with conditions typical of automotive particulate filters, building upon the findings of Thieringer et al [10, 20].

To precisely control the temperature of the oxidation gas within the model filter channel, the synchronization of the oven temperature, the gas flow rate, and the heating plate temperature, which directly heats the filter channel from below, is critical. PT100 temperature sensors are employed at both the inlet and outlet of the channel to continuously monitor and adjust the temperatures during the process. The oven operates at 1473 K, while an inert nitrogen gas flow is used for preheating the system, minimizing heat loss and preventing the gas from cooling significantly as it moves from the oven to the channel. The transition pipe to the filter is further heated with a heating wire and thermally insulated to preserve heat. The heating plate is maintained at 1043 K, ensuring an oxidation gas temperature of 823 K during the regeneration process. The stainless-steel filter holder is also thermally insulated with high-temperature gaskets. Throughout the entire regeneration process, the temperature difference between the inlet and outlet of the channel remains below 10 K, enabling a stable and uniform temperature distribution within the channel.

Image Analysis The experiments were observed using a high-speed camera (CP90-25P-M72, Optronis GmbH) positioned perpendicular to the model filter channel (MFK) through a quartz glass window. Lighting was provided by two LED panels (GSVitec, MultiLed G8, QT+G8) with a luminous flux of ϕ = 12,000 lm and a power output of P = 150 W each. The camera, equipped with a Zeiss Macro lens (Milvus 2/100M), operated at an exposure time of 1/100000 s and an image format of 5120 px x 200 px. During regeneration, a frame rate of 100 fps was initially set, which was increased to 1000 fps once the soot layer began to break up visibly.

Custom Python scripts were developed to perform image analysis with a focus on identifying layer break-up in images and particle movement in video footage obtained from the high-speed camera.

For layer break-up image analysis, the analysis workflow includes image pre-processing, segmentation, and geometric evaluation of regions of interest (ROIs). The preprocessing phase enhances critical image features through contrast, brightness, exposure and blackness adjustments, grayscale conversion, and Gaussian smoothing to reduce background noise. Threshold-based segmentation using Otsu's method binarizes the images to separate particle-like structures from the background. Morphological operations such as erosion, dilation, and opening further refine the binary images by removing residual noise and isolating individual features. Each computational step relies on established image processing methods [24, 25, 26]. Figure 4 illustrates the binarization process as part of the image analysis methodology. The original image (a) serves as the input, showing a soot layer with low-contrast features. To enhance visibility and isolate regions of interest, the image is processed using the following parameters: a minimum area of 20 px ≈ 0,015 mm^2), a kernel size of 3x3, Gaussian smoothing with a kernel size of 5x5, two morphological iterations (erosion step followed by dilation, repeated twice), and Otsu's thresholding method. Contrast and brightness range from 0 to 300, with 100 indicating no change. Blackness, a gamma-like factor from 0 to 2, has a neutral setting at 1.0. Exposure, which also ranges from 0 to 2 and is neutral at 1.0, scales intensities multiplicatively. To accentuate low-contrast soot features, the following settings were applied: contrast = 150, brightness = 300, blackness = 0.7, and exposure = 2. The resulting binarized image (b) highlights the soot structures by separating them from the background.

Once segmentation is complete, connected regions of interest (ROIs) are identified and their geometric properties including area, width, height, and centroid coordinates are extracted. These properties are converted from pixel dimensions to physical units (µm) for precise quantification. The structured workflow enables accurate detection, quantification, and visualization of layer break-up, providing a systematic and reproducible approach to image-based analysis. Using a sequence of images over the regeneration period, visual layer break-up can be tracked and quantified over time. The time until a 10 % visual reduction in layer surface area is represented by τ_{90}, which defines in this study the onset of layer break-up.

A Monte Carlo–based method [27] is employed to quantify measurement uncertainties, anchored on the Otsu threshold method. First, the automatic threshold is

FIGURE 4 (a) Example of the binarization process applied to an original image, (b) The resulting binarized image.

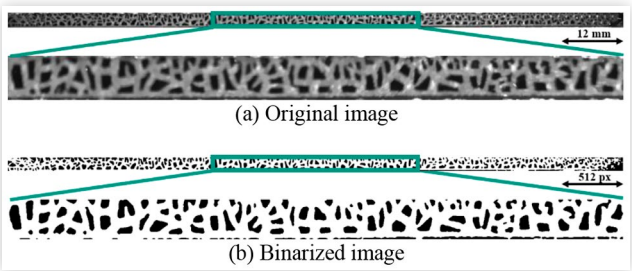

determined via Otsu for each image region. Next, this baseline threshold is varied as well as the values for blackness and exposure by ± 5 % across multiple runs (for 20 Monte Carlo iterations), and each run re-segments the particle regions. The total segmented area and particle count are recorded for every run, and their standard deviations serve as measures of error in area and particle count, respectively.

For particle detection and tracking, the preprocessing of video files also include contrast and brightness setting adjustment to enhance critical features. The video is processed frame by frame. Frame differencing compares consecutive frames to isolate changes, newly introduced or moving particles, against a mostly static background. The differenced frames are then converted to grayscale, and thresholding and morphological operations further refine the detection by removing noise and isolating particle-like features. Once segmented, geometric properties such as centroids, bounding boxes, and shape descriptors are computed for each detected object. To track particles across frames, the Hungarian algorithm assigns detected objects to existing tracks. Kalman filters predict new object positions, while new tracks are initiated for unassigned detections. Alternatively, the tracks can be tracked manually in the difference images. Figure 5 illustrates the particle tracking method. The top image shows the complete frame, while the sequence below displays selected regions from sequential frames, including difference images (0-1, 1-2) and individual frames (0, 1, and 2). Particles are highlighted with green circles, and their trajectories are visualized with orange lines, demonstrating the identification and tracking of particle motion over time. The outputs include annotated video frames, difference images, and extracted particle trajectories. Key data, such as object positions, sizes, and temporal evolution, are saved in spreadsheet format for further analysis. This systematic tracking procedure provides particle trajectories, enabling the quantitative study of particle motion and dynamics during regeneration processes. Although this approach is effective, it has some limitations. During regeneration, millions of frames are recorded, while relevant rearrangements occur only in a few frames. To eliminate false detections, the detected relocations are manually verified afterwards. Because complete manual evaluation is very time-consuming, further code development will improve the isolation of relocating structures under low-contrast conditions and increase automation. Consequently, the detected rearrangements reported here should be viewed as a minimum number.

FIGURE 5 Example illustrating the particle tracking method on a detachment event. The top image shows the complete frame, while the series of images below displays selected region from sequential frames (0, difference frame 0-1, frame 1, difference frame 1-2, and frame 2). Particles are highlighted with green circles, and their trajectories are indicated with orange lines.

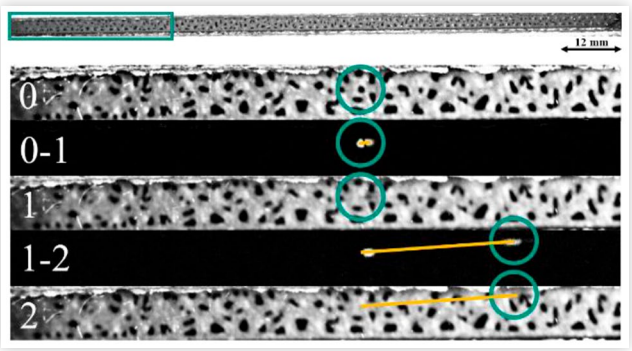

Results and Discussion

Progression of the Regeneration

To provide information on the regeneration behavior of the model filter channel, Figure 6 illustrates the progression of the regeneration process for PropSoot (a) and CB (b) over a period of 90 min. The image sequences depict the temporal development of soot layer break-up and oxidation in time intervals of 15 min, starting from the beginning of regeneration (0 min) to 90 min. At the initial time point (t_0 = 0 min), the inlet channel surface appears uniformly black, indicating a closed soot layer. For PropSoot (Figure 6a), the soot layer exhibits a uniform layer break-up during progressing regeneration, with visibly separated particle structures. In contrast, the CB layer (Figure 6b) shows a slower and less uniform progression, with larger structural sizes that persist throughout regeneration. By the 30 min mark, it becomes evident that the CB layer in this experiment oxidizes more rapidly in the central region of the channel compared to the inlet and outlet regions. After 45 min, the CB layer exhibits visible separation of the particle structures along the channel, with the structures shrinking over the remaining regeneration time.

Measurements of process parameters are presented in Figure 7 for both PropSoot (a) and CB (b). These graphs show the regeneration temperature T_{reg} and normalized differential pressure $\Delta p_{channel}$ as functions of time. For

FIGURE 6 Image sequence of the regeneration process for PropSoot (a) and CB (b), illustrating the progression from the start of regeneration (0 min) to 90 min. (An enlarged version of the Images can be found in Appendix A, Figure 17).

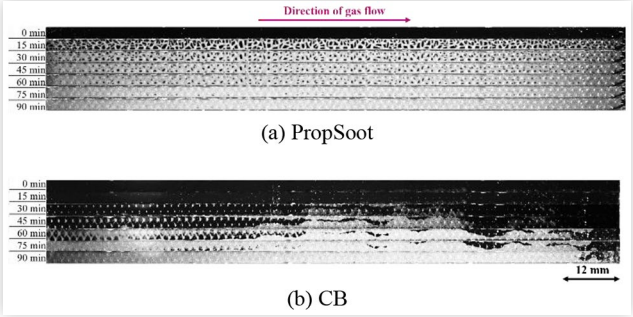

FIGURE 7 Progression of the process parameters during regeneration of the model filter channel with PropSoot (a) and CB (b) at a regeneration temperature of 823 K, and an air flow velocity of 60 m/s with an oxygen content of 21 vol. %.

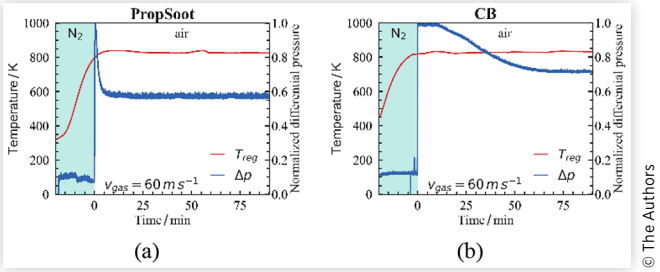

PropSoot (Figure 7a), the temperature remains stable at $T_{reg} \approx 823$ K. The normalized differential pressure $\Delta p_{channel}$ continuously decreases, indicating an ongoing removal of soot from the filter channel. In the case of CB Figure 7b), the regeneration temperature is similarly maintained at $T_{reg} \approx 823$ K. However, the decrease in $\Delta p_{channel}$ is more gradual, underscoring the lower reactivity of CB compared to PropSoot. These trends clearly illustrate the differences in oxidation behavior and layer dynamics between the two particle systems during the regeneration process.

Visual Layer Break-Up

Using the previously described image analysis method, the progression of soot layer break-up and the evolution of structural sizes during re-generation were quantified. The results, as shown in Figure 8, illustrate the layer reduction over time for PropSoot (a) and CB (b), segmented into three channel regions: inlet (1/3), middle (2/3), and outlet (3/3). The y-axis represents the fraction of the black surface area remaining, while the x-axis shows the time in minutes. For PropSoot, a rapid reduction is observed, with the reduction in soot layer area being uniform across all three channel regions. In contrast, the reduction for CB is slower and less homogeneous, with noticeable delays in the front and outlet regions. A direct comparison of total layer reduction for both soot types is shown in Figure 9. For PropSoot, the onset of layer break-up, defined as a 10 % reduction in black surface area fraction, occurs rapidly at approximately 2 min. This indicates a fast reaction from the very beginning. In contrast, the onset for CB is delayed, occurring around 29 min, underscoring its lower reactivity. PropSoot exhibits a faster and more complete layer reduction, achieving near-total oxidation within 60 min. CB, on the other hand, has residual structures persisting even after 90 min. Calculations of the normalized mass loss for both types of soot, based on the kinetic data from the TPO (see Figure 18 in Appendix A) at 823 K, suggest that PropSoot should be fully regenerated after 60 min, whereas CB would only achieve about 50 % conversion within the same timeframe. Any deviations between purely kinetic predictions

FIGURE 8 Comparison of layer reduction over time for PropSoot (a) and CB (b) across different channel regions: inlet (1/3), middle (2/3), and outlet (3/3). The total layer reduction for each soot type is also shown.

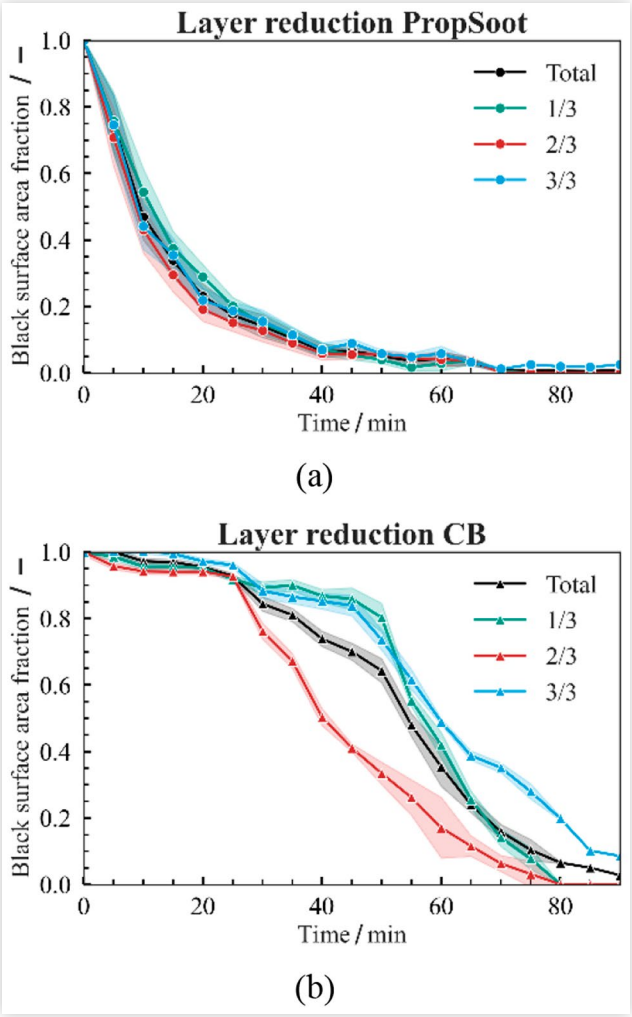

FIGURE 9 Comparison of total layer reduction over time and marking the onset of layer break-up.

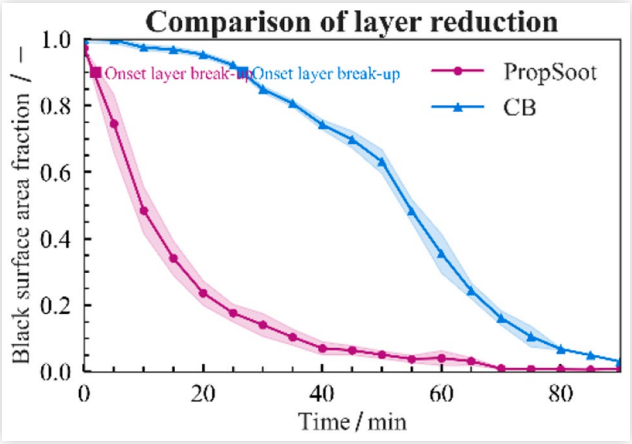

and the observed behavior may stem from altered mass and heat transfer in the dense soot bed. Nonetheless, these results align almost perfectly with the kinetics inferred from the TPO experiments. The progression of structural numbers during regeneration is depicted in Figure 10. For PropSoot, the number of identifiable structures peaks at approximately 15 min with 310, followed by a rapid decrease as the soot particles oxidize. CB shows a delayed and less pronounced peak, with a more gradual decrease over time, with distinguishable areas forming later and in significantly fewer numbers. The structural sizes are also larger compared to PropSoot.

The cumulative particle size distributions for PropSoot and CB at different time points are shown in Figure 11. As regeneration progresses, the distributions shift toward smaller sizes. By 60 min, most of the larger PropSoot structures have shrunk and the smaller particles have completely oxidized. However, CB structures form fewer larger cohesive structures.

The image analysis reveals that PropSoot undergoes faster and more uniform layer break-up, with smaller and more rapidly oxidizing structures compared to CB. These differences are attributed to variations in soot reactivity and dispersity, providing information on the dynamics of particulate filter regeneration with different types of soot.

FIGURE 10 Comparison of structural number progression over time.

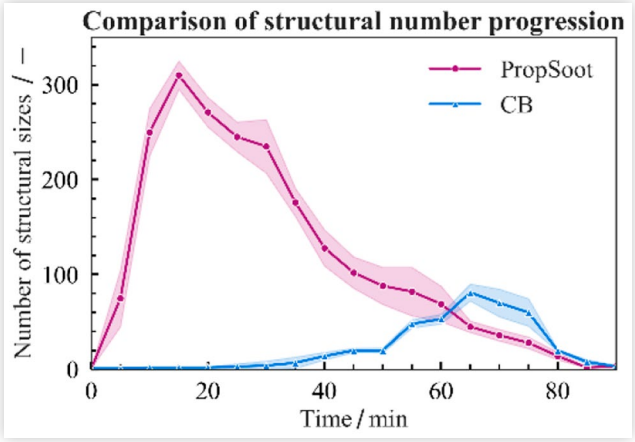

FIGURE 11 Cumulative distribution Q_0 of structural sizes ($x_{eq,str}$ for PropSoot at different regeneration times (15 min, 30 min, 45 min, and 60 min) and CB at different regeneration times (45 min, and 60 min), obtained by the image analysis of individual frames at the respective time.

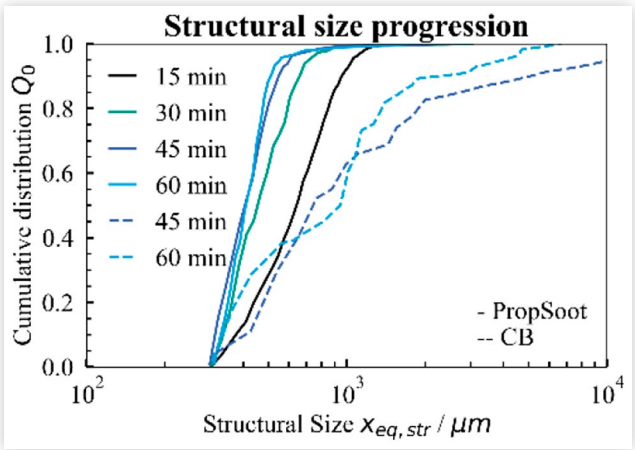

Relocations of Particulate Structures

Using the previously described image analysis method for particle detection and tracking, the spatial and temporal redistribution of detached soot structures during the regeneration process was analyzed. The results are presented in Figure 12-16. Figure 12 illustrates the spatial distribution of particle detachment and deposition events for PropSoot (a) and CB (b).

In the case of PropSoot, the detachment events are widely distributed across the channel length, with a higher density in the direction of the channel inlet. Depositions, on the other hand, occur mainly near the outlet; the particles are transported to the end of the channel with the gas flow at these process parameters. For CB, significantly fewer detachment and deposition events were observed. The equivalent diameters of detached particles were measured at approximately 450, 243, 111, and 45 µm. For three of these particles, only the deposition could be identified at 33 min regeneration time, occurring approximately two-thirds along the channel length on

FIGURE 12 Spatial distribution of particle detachment and deposition events along the channel length for PropSoot (a) and CB (b), detachment events (red) and depositions (green).

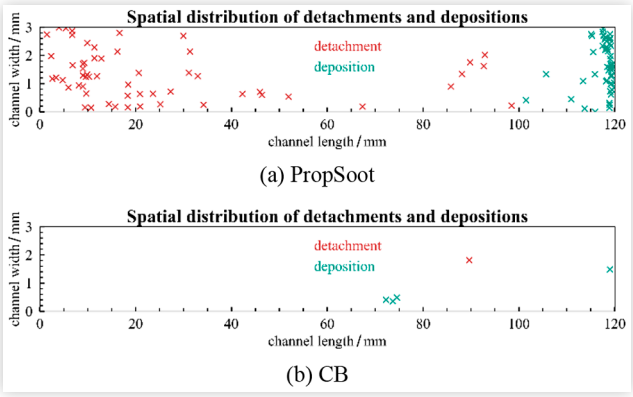

FIGURE 13 Image sequence highlighting CB structure deposition at 33 min.

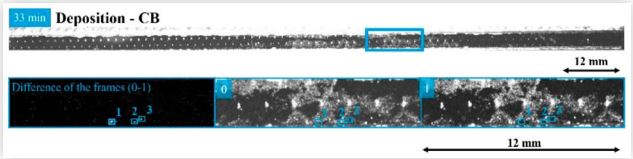

FIGURE 14 Image sequence highlighting PropSoot structure detachment, transport, deposition and hitting of the end of the channel at 16 min.

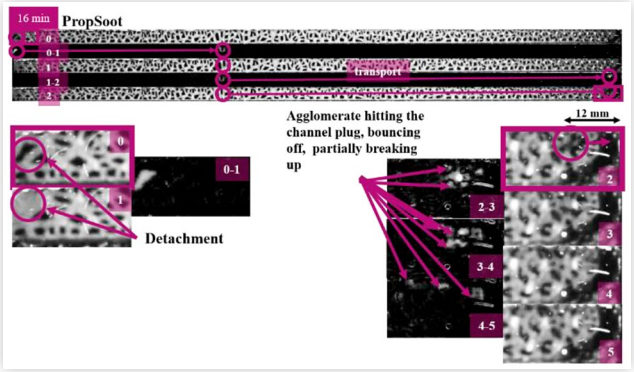

FIGURE 15 Relocation tracks of PropSoot structures with velocity gradient along the channel length. The color gradient indicates particle structure velocity.

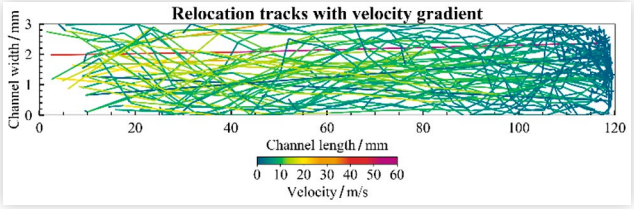

larger structures as shown in Figure 13. Due to the persistent black soot layer on the filter channel surface, the exact origin or process of detachment of these particles could not be determined.

The particle size of the relocated PropSoot particles varied between 50 and 1000 µm, a range consistent with the observations made by Sappok et al. [11] and Thieringer et al. [10].

The relocation tracks of PropSoot particles, shown in Figure 15, reveal the velocity-dependent movement of detached structures along the channel. Particle structures detaching near the channel inlet and in the center of the channel exhibit higher velocities, decreasing toward the end of the channel. Although some particles in the central region still exhibit lower speeds. In contrast, lower velocities dominate along the channel edges, and overall flow speeds decrease toward the channel outlet. The gradient in velocity further emphasizes the influence of position in the channel on particle structure transport. The image sequence of a representative PropSoot structure detaching and relocating at 37 min is shown in Figure 19 in Appendix A. Some particles hit the channel wall or the channel plug, bounce off, are partially broken up and slow down their movement significantly as seen in an example relocation of a PropSoot structure in Figure 14. This also matches the observations made by Thieringer et al. [10, 28] under similar experimental conditions for PropSoot.

FIGURE 16 Heat matrix showing the spatial and temporal distribution of detachment events (PropSoot) along the channel. The color gradient represents the average time of detachment, while the numbers indicate the total counts of detachment events per bin.

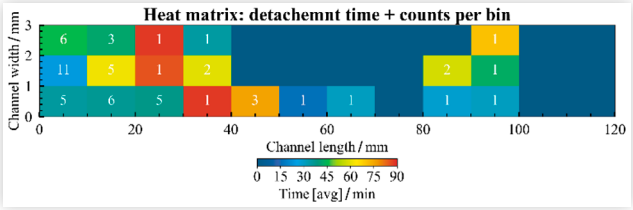

Figure 16 provides a heat matrix of particle structure detachment events, showing the temporal and spatial distribution of detachment counts within the channel. The reported time represents the mean value computed from all individual event times within a given bin. For PropSoot, detachment events are concentrated within 60 min and are most frequent in the inlet region of the channel. The number of detachments decreases significantly towards the end of the channel, so that only individual events take place there, usually at an advanced regeneration time. The analysis highlights clear differences in the dynamics of particle structure relocations between PropSoot and CB. PropSoot exhibits a more active and dynamic regeneration process, with more relocations and significant deposition near the outlet of the channel. In Contrast, CB shows limited transport of structural sizes, with detachment and deposition events confined to rare specific events occurring at a slower rate.

Conclusion

The use of high-speed imaging combined with advanced image analysis allows the quantification of layer break-up, structural size evolution, and particle relocation dynamics under controlled experimental conditions. The regeneration dynamics of highly reactive PropSoot and less reactive CB layers within a model filter channel are highlighting significant differences. Key findings are summarized in Table 2 and indicate that PropSoot undergoes more rapid and uniform oxidation, accompanied by a high number of particle structure detachment and deposition events. In contrast, CB exhibits slower and less homogeneous oxidation behavior, persistent large structures, and fewer (close-to-zero) detachment events. These differences underscore the importance of soot reactivity and particle dispersity in influencing regeneration efficiency and kinetics. The results provide a foundation for optimizing particulate filter operating conditions, contributing to more effective emission control strategies.

TABLE 2 Overview of the results.

	PropSoot	CB
Characterization		
CMD / nm	26	101
C:H ratio	-	11,4
T_{max} / K	817	902
$k_{0,ox}$ / s^{-1}	$8.05 \cdot 10^5$	$3.59 \cdot 10^6$
n	1.39	0.95
Ea / kJ/mol	137	162
Layer break-up		
Onset of layer break-up τ_{90} / min	2.18	29.5
Maximum number of structural sizes per frame	310	81
Relocation of particle structures		
Number of relocations	≥ 58	≥ 4
Time of 1st relocation / min	8.74	33
$x_{relocations}$ / µm	50..1000	45..450

Recommendation

Future work will focus on refining detection methods to improve the quantification of particle relocations. Moreover, by varying the particulate systems and the reactive-inert particle ratio, the impact of particulate properties and their reactivity on the resulting ash deposition patterns following the regeneration of the particulate filter will be examined. Expanding the experimental scope will allow for a broader understanding of soot behavior. Future studies should include a wider variety of soot types with differing nanostructural properties and reactivities to generalize the findings. Additionally, varying gas flow rates, regeneration temperatures, reactive-to-inert particle ratios and the oxidation gas NO_2 will help simulate real-world conditions more effectively, offering deeper insights into the behavior of soot layers during regeneration.

From a practical perspective, the insights gained in this study could be applied to optimize particulate filter operation. Specifically, the results could improve the development of wall-flow filters with advanced channel structures and regeneration protocols. Moreover, investigating the effects of renewable fuels and biomass-derived soot on regeneration efficiency aligns with the increasing focus on sustainable technologies.

References

1. European Parliament, "Directive (EU) 2024/2881 of the European Parliament and of the Council of 23 October 2024 on Ambient Air Quality and Cleaner Air for Europe (Recast)," 2024, http://data.europa.eu/eli/C/2023/251/oj.
2. Dittler, A., "The Application of Diesel Particle Filters—From Past to Present and Beyond," *Top Catal.* 60, no. 3–5 (2017): 342-347, doi:10.1007/s11244-016-0621-z.
3. Karin, P., Cui, L., Rubio, P., Tsuruta, T. et al., "Microscopic Visualization of PM Trapping and Regeneration in Micro-Structural Pores of a DPF Wall," *SAE Int. J. Fuels Lubr.* 2, no. 1 (2009): 661-669, doi:10.1016/j.jaerosci.2016.01.009.
4. Jiang, J., Gong, J., Liu, W., Chen, T. et al., "Analysis on Filtration Characteristic of Wall-Flow Filter for Ash Deposition in Cake," *J. Aerosol. Sci.* 95 (2016): 73-83, doi:10.1016/j.jaerosci.2016.01.009.
5. Kittelson, D.B., "Engines and Nanoparticles: A Review," *J. Aerosol. Sci.* 29, no. 5 (1998): 575-588, doi:10.1016/j.jaerosci.2016.01.009.
6. Dittler, A., "Ash Transport in Diesel Particle Filters," SAE Technical Paper 2012-01-1732 (2012), https://doi.org/10.4271/2012-01-1732.
7. Frank, R.W. and Hardenberg, H.O., "Reduction of Particulate Emission from the Break-in Facilities of a Heavy-Duty Engine Plant by Means of Ceramic Monolith Traps," SAE Technical Paper 850268 (1985), https://doi.org/10.4271/850268.
8. Konstandopoulos, A.G. and Johnson, J.H., "Wall-Flow Diesel Particulate Filters—Their Pressure Drop and Collection Efficiency," SAE Technical Paper 890405 (1989), https://doi.org/10.4271/890405.
9. Gerd, G. and Patrick, M., "Prediction of Pressure Drop in Diesel Particulate Filters Considering Ash Deposit and Partial Regenerations," SAE Technical Paper 2004-01-0158 (2004), https://doi.org/10.4271/2004-01-0158.
10. Thieringer, J.R.D., Werling, H., Meyer, J., and Dittler, A., "In Situ Tracking of Break-up, Resuspension, and Transport of Reactive Particle Structures in a Single Wall-Flow Filter Channel," *Emission Control Science and Technology* (2023): 149-165, doi:10.1007/s40825-023-00228-x.
11. Sappok, A., Govani, I., Kamp, C., Wang, Y. et al., "In-Situ Optical Analysis of Ash Formation and Transport in Diesel Particulate Filters During Active and Passive DPF Regeneration Processes," *International Journal of Fuels and Lubricants* 6, no. 2 (2013): 336-349, doi:10.2307/26273010.
12. Hafen, N., Marquardt, J.E., Dittler, A., and Krause, M.J., "Simulation of Particulate Matter Structure Detachment from Surfaces of Wall-Flow Filters for Elevated Velocities Applying Lattice Boltzmann Methods," *Fluids* 8, no. 3 (2023), doi:10.3390/fluids8030099.
13. Lapuerta, M., Hernández, J.J., and Oliva, F., "Strategies for Active Diesel Particulate Filter Regeneration Based on Late Injection and Exhaust Recirculation with Different Fuels," *International Journal of Engine Research* 15, no. 2 (2014): 209-221, doi:10.1177/1468087412468584.
14. Stanmore, B.R., Tschamber, V., and Brilhac, J.F., "Oxidation of Carbon by NOx, with Particular Reference to NO2 and N2O," *Fuel* 87, no. 2 (2008): 131-146, doi:10.1016/j.fuel.2007.04.012.
15. Hagen, F. et al., "Why Soot is not Alike Soot: A Molecular/Nanostructural Approach to Low Temperature Soot Oxidation," *Flow Turbul Combust* 106, no. 2 (2021): 295-329, doi:10.1007/s10494-020-00205-2.
16. Hays, M.D. and Vander Wal, R.L., "Heterogeneous Soot Nanostructure in Atmospheric and Combustion Source Aerosols," *Energy & Fuels* (2007): 801-811, doi:10.1021/ef060442h.

17. Liati, A., Spiteri, A., Eggenschwiler, P.D., and Vogel-Schäuble, N., "Microscopic Investigation of Soot and Ash Particulate Matter Derived from Biofuel and Diesel: Implications for the Reactivity of Soot," *Journal of Nanoparticle Research* 14, no. 11 (2012), doi:10.1007/s11051-012-1224-7.
18. Levenberg, K., "A Method for the Solution of Certain Non-Linear Problems in Least Squares," *Q Appl Math* 2, no. 2 (1944): 164-168, https://about.jstor.org/terms.
19. Marquardt, D.W., "An Algorithm for Least-Squares Estimation of Nonlinear Parameters," *Journal of the Society for Industrial and Applied Mathematics* 11, no. 2 (1963): 431-441, https://www.jstor.org/stable/2098941.
20. Thieringer, J.R.D., "Umlagerungsvorgänge von Partikelstrukturen in Wandstromfiltern," Karlsruher Institut für Technologie (KIT), 2024, doi:10.5445/IR/1000170569.
21. Ess, M.N. et al., "Reactivity and Structure of Soot Generated at Varying Biofuel Content and Engine Operating Parameters," *Combust Flame* 163 (2016): 157-169, doi:10.1016/j.combustflame.2015.09.016.
22. Lindner, S., Massner, A., Gärtner, U., and Koch, T., "Impact of Engine Combustion on the Reactivity of Diesel Soot from Commercial Vehicle Engines," 2015, SAGE Publications Ltd., doi:10.1177/1468087414563360.
23. Koch, S. et al., "Influence of Global Operating Parameters on the Reactivity of Soot Particles from Direct Injection Gasoline Engines," *Emission Control Science and Technology* 8, no. 1–2 (2022): 9-35, doi:10.1007/s40825-022-00211-y.
24. Otsu, N., "A Threshold Selection Method from Gray-Level Histograms," *IEEE Trans Syst Man Cybern* 9, no. 1 (1979): 62-66.
25. Jähne, B., *Digitale Bildverarbeitung* (Berlin: Springer, 2002)
26. Gonzalez, R.C. and Woods, R.E., *Digital Image Processing* (Upper Saddle River: Prentice Hall, 2008)
27. Metropolis, N. and Ulam, S., "The Monte Carlo Method," *Journal of the American Statistical Association* 44, no. 247 (1949): 335-341.
28. Thieringer, J.R.D., Hafen, N., Meyer, J., Krause, M.J. et al., "Investigation of the Rearrangement of Reactive–Inert Particulate Structures in a Single Channel of a Wall-Flow Filter," *Separations* 9, no. 8 (2022), doi:10.3390/separations9080195.

Nomenclature

α - Fractional mass conversion

$d\alpha/dT$ - Differential mass loss rate (K^{-1})

T - Temperature (K)

T_{max} - Temperature of maximum oxidation rate (K)

k_{ox} - Oxidation rate coefficient (K^{-1})

$k_{0,ox}$ - Pre-exponential factor (s^{-1})

E_a - Activation energy (kJ/mol)

n - Reaction order

R - Universal gas constant (8.314 J/mol K)

x_{eq} - Equivalent particle size (μm)

Q_0 - Cumulative particle size distribution

τ_{90} - Time until 10 % reduction in black surface area (min)

$\frac{\Delta p_{channel}}{\Delta p_{max}}$ - Normalized differential pressure

β - Heating rate (K/min}

c_{O2} - Oxygen concentration (vol. %)

c_{NO2} - Nitrogen concentration (vol. %)

ϕ - Luminous flux (lm)

P - Power (W)

Contact Information

Ole Desens
Institute of Mechanical Process Engineering and Mechanics
Karlsruhe Institute of Technology
ole.desens@kit.edu

Acknowledgments

The authors are very grateful to the Deutsche Forschungsgemeinschaft (DFG, German Research Foundation) for financial support within the project 438308378. During the preparation of this work the authors used "ChatGPT4o" and "DeepL Write" in order to refine the language with grammar and punctuation corrections. After using these tools the authors reviewed and edited the content as needed and take full responsibility for the content of the publication. Parts of this work were presented at FILTECH 2024.

Definitions, Acronyms, Abbreviations

CB - Carbon Black

CMD - Count Median Diameter

DPF - Diesel Particulate Filter

fps - Frames per second

HRTEM - High-resolution transmission electron microscopy

PropSoot - Propane Soot

SEM - Scanning Electron Microscope

OPF/GPF - Gasoline particulate filter

PM - Particulate matter

PropSoot - Propane Soot

ROI - Region of interest

SEM - Scanning Electron Microscope

TPO - Temperature programmed oxidation

Appendix A

TABLE 3 Operating conditions.

PropSoot - Jing Soot generator		CB - ring disperser	
Gas	**Flow rate / l/min**	**Parameter**	**Value**
Propane	0.05	Ring velocity / %	10
Quench gas (N_2)	2.0	Height of the scraper / mm	5.74
Oxidation air	1.0	Pre-pressure / mbar	1.6
Mixing gas (N_2)	0.01	Ring width / mm	1.2
Dilution air	0.01	Rate of the screw conveyor / -	4/6

$$\alpha(t) = \left(\alpha_0^{1-n} - (1-n)k_{ox} \cdot t\right)^{\frac{1}{1-n}}, \text{if } n \neq 1, \quad (2)$$

where α_0 is the initial value of the conversion (set to 1 for a fully reactive fraction), k_{ox} is the reaction rate constant, and n is the reaction order. The rate constant k is computed according to Equation 3,

$$k_{ox} = k_{0,ox}\, exp\left(-\frac{E_a}{RT}\right), \quad (3)$$

with the pre-exponential factor $k_{0,ox}$, the activation energy E_a, the universal gas constant R, and the absolute temperature T.

FIGURE 18 Theoretical oxidation kinetics based on the fitted TPO parameters showing the fractional mass conversion α as a function of time for PropSoot (E_a = 137 kJ/mol}, T = 823 K, n = 1.39) and CB (E_a = 162 kJ/mol, T = 823 K, n = 0.95). In order to describe the oxidation kinetics, the fractional mass conversion α(t) is defined as

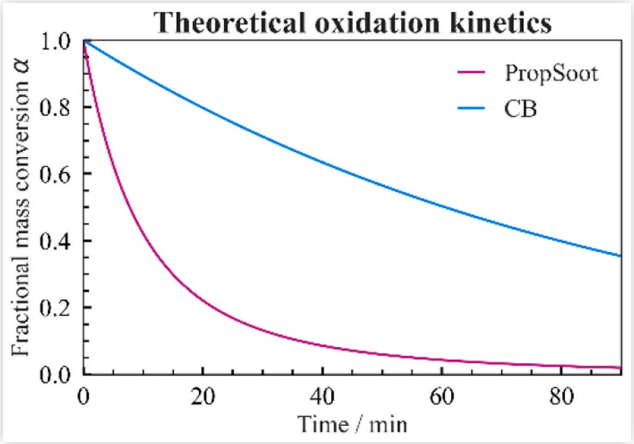

FIGURE 17 Image sequence of the regeneration process for PropSoot (a) and CB (b), illustrating the progression from the initiation of regeneration (0 min) to 90 min.

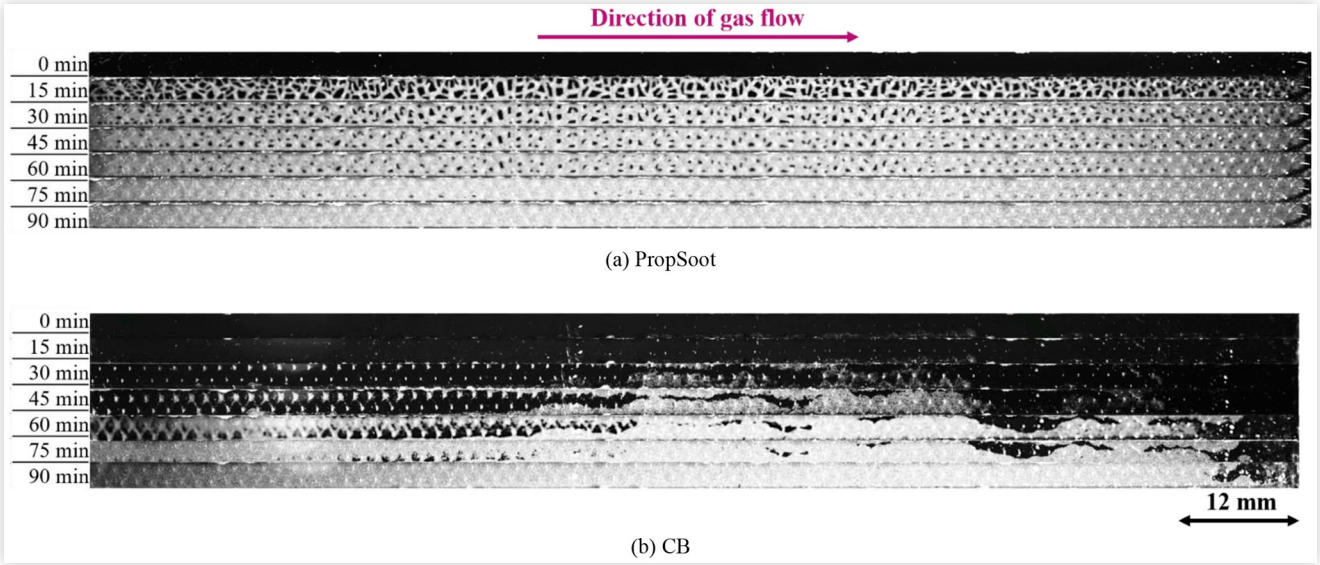

FIGURE 19 Representative image sequence of a PropSoot structures detaching and relocating at 37 min.

ISSN 0148-7191